“Oxygen quenching” in Eu-based thermographic phosphors

DOI:
10.1016/j.snb.2017.07.092

Document Version
Accepted author manuscript

“Oxygen Quenching” in Eu-based Thermographic Phosphors: Mechanism and Potential Application in Oxygen/Pressure Sensing

Lixia Yang[1,2], Xiaofeng Zhao[1,2,*], Di Peng[1,3,*] , Xiao Shan[1,2], Fangwei Guo[1,2], Yingzheng Liu[1,3], , Ping Xiao[4,2]

1 Gas Turbine Research Institute, Shanghai Jiao Tong University, Shanghai 200240, China

2 Shanghai Key Laboratory of Advanced High-temperature Materials and Precision Forming, Shanghai Jiao Tong University, Shanghai, 200240, China

3 Key Lab of Education Ministry for Power Machinery and Engineering, School of Mechanical Engineering, Shanghai Jiao Tong University, Shanghai, 200240, China

4 School of Materials, University of Manchester, Grosvenor Street, Manchester M1 7HS, UK

Abstract

The effect of ambient oxygen concentration on thermographic phosphor thermometry was investigated to uncover the “oxygen quenching” mechanism of Eu-based phosphors using a lifetime-based measurement system. The phosphors being studied were the Eu doped yttria stabilized zirconias (YSZs) with Y^{3+} concentrations of 0, 8, 12 and 57 mol%, having monoclinic, tetragonal, cubic and δ crystalline lattice, respectively. To vary the ambient oxygen concentration, three different gas phases (air, oxygen and nitrogen with methane) were used. It was found that the phosphorescent lifetimes and intensities of all four phosphors were sensitive to the ambient oxygen concentration, while the reference phosphor, Y_2SiO_5:Eu, was not influenced. The “oxygen quenching” phenomenon observed in Eu-doped YSZs was attributed to the oxygen vacancies in the phosphors. In addition, the four YSZ:Eu phosphors exhibited different sensitivity to ambient oxygen concentration. The oxygen sensitivity was found to be closely related to the site symmetry of Eu^{3+}, which was previously determined by

* xiaofengzhao@sjtu.edu.cn (Xiaofeng Zhao).
idgnep8651@sjtu.edu.cn (Di Peng).

the phosphorescent spectra. The site symmetry of Eu^{3+} strongly affected the charge-transfer states and therefore determined the non-radiative decay rate. The current findings provided guidance for the phosphor selection and sensor design for oxygen/pressure sensing in high-temperature environment.

Keywords: thermographic phosphor; oxygen quenching; oxygen vacancy; site symmetry

---

1. Introduction

Remote temperature sensing technology using thermographic phosphor has been developed and successfully applied for monitoring and analyzing the high-temperature and highly corrosive environments [1-3]. A thermographic phosphor typically consists of a ceramic host doped with a lanthanide (rare earth elements) to act as a luminescence centre. To facilitate surface measurements, the phosphor is applied as a thin coating on the surface of interest. After being excited with a pulsed light, the phosphors exhibit exponentially decaying luminescence, and the decay time decreases as temperature increases. One of the recent applications of thermographic phosphor is the in-situ temperature measurement in thermal barrier coatings (TBCs) used in gas turbines [4-6]. During gas turbine services as well as in many other applications of combustion engines, motors or generators, it is very likely that the thermographic phosphors could be exposed to varied oxygen concentrations and surface pressures. For reliable phosphor thermometry, the phosphorescent properties should be independent of these changes. If not, the phosphors can act as ambient oxygen/pressure sensors in harsh environment with temperature over 1000 ℃ [7], where it is impossible to apply pressure-sensitive paints (PSP) which typically contain organic luminescent molecules embedded in a polymer binder [8]. Therefore, it is important to study the effect of the ambient oxygen concentration on the luminescent properties of phosphors.

Surface pressure/oxygen concentration measurements using PSP are based on the

excited state of the luminescent molecules are deactivated upon collision with oxygen molecules through a non-radiative energy transfer process, i.e., the luminescence is quenched by oxygen [8]. Inorganic thermographic phosphors have been generally considered to be insensitive to oxygen, but several studies showed that the phosphorescent properties of certain phosphors were affected by oxygen concentration and/or pressure. Feist *et al*. first investigated the oxygen quenching of the luminescence of Y_2O_3:Eu as well as YAG:Dy at ambient pressure [9]. They found that varying the oxygen concentration in a calibration furnace between 5% and 21% resulted in an increase of the uncertainty of lifetime-based temperature measurements by 0.5% to 1%. But no absolute change in phosphor lifetime was reported. A subsequent work by Brübach *et al*. [10] demonstrated that both of the Mg_4FGeO:Mn and La_2O_2S:Eu thermographic phosphors were not influenced by gas composition variations, while Y_2O_3:Eu phosphor showed a strong sensitivity on the oxygen concentration of surrounding gas phase. More recently, Shen *et al.* [11] investigated the Eu doped yttria stabilized zirconia (YSZ) as an embedded layer in TBCs exposed to reducing atmosphere: the luminescence intensity was decreased but the lifetime was unaffected by the reduction of pressure. Up to now, the knowledge about "oxygen quenching" of thermographic phosphor is still limited, and no attempt has been made to reveal the underlying mechanism in spite of its importance.

The principal objective for this work is to investigate the influence of ambient oxygen concentration on the phosphorescent lifetime and explore its mechanisms. Based on the previous works, Eu^{3+} was selected as a luminescence center with the same concentration (1 mol%) for all specimens. Since the main differences between Y_2O_3:Eu and YSZ:Eu are the yttria concentration and the crystal structure, four YSZ materials were selected as ceramic hosts: ZrO_2 without $YO_{1.5}$ (monoclinic structure); YSZ with 8 mol% $YO_{1.5}$ (tetragonal structure); YSZ with 12 mol% $YO_{1.5}$ (cubic structure) and YSZ with 57 mol% $YO_{1.5}$ (i.e., $Zr_3Y_4O_{12}$, δ structure). The phosphors were prepared using sol-gel method and then deposited using air plasma spraying (APS) process on the bond coated Hastelloy substrate, which are widely used as the bond coat/substrate

system in TBCs. The crystal structures of the phosphor layers were identified by X-ray diffraction (XRD). Then the phosphorescent properties, including spectrum, lifetime and intensity, were characterized in a pressure chamber using an optical measurement system. The relationship between the phosphorescent properties and the site symmetry of Eu^{3+} was identified, and the effect of the ambient oxygen concentration on the temperature dependent phosphorescent lifetimes and intensities of Eu^{3+} in these four phosphor layers was investigated. The mechanism of the "oxygen quenching" was discussed in detail, which could serve as basis for future development of oxygen/pressure sensitive phosphors.

2. Experiment

The 0YSZ:Eu, 8YSZ:Eu, 12YSZ:Eu and $Zr_3Y_4O_{12}$:Eu phosphor powders were prepared using sol-gel method by controlling Y^{3+}-doping concentrations of 0, 8, 12 and 57 mol%, respectively. The content of Eu^{3+} was 1 mol% for all specimens. The sol-gel method was selected for the preparation of the materials to avoid segregation of the cations and ensure molecular mixing of the dopant into the ceramic host. The starting materials for the powder preparations included $ZrO(NO_3)_2 \cdot 3H_2O$ (99.99% metals basis), Eu_2O_3 (99.99%), Y_2O_3 (99.99%), HNO_3 and citric acid. A procedure for the powder synthesis is described as follows: Eu_2O_3 and Y_2O_3 were weighed according to the target composition. They were first dissolved in nitric acid under heating. After the Eu_2O_3 and Y_2O_3 were completely dissolved, the excess nitric acid was removed at elevated temperature. Then de-ionized water was adder to obtained $Eu(NO_3)_3$ and $Y(NO_3)_3$ solution. Meanwhile citric acid was added to the above solution as chelated agent for the metal ions. The molar ratio of the total metal ions to the citric acid was 1:2. Subsequently, $ZrO(NO_3)_2 \cdot 3H_2O$ were dissolved in a de-ionized water while stirring. After this procedure, polyethylene glycol (molecular weight 20,000) as cross-linking agent was also added. At the end, the mixed solution was slowly dropped into rare earth solution with magnetic stirring, and the highly transparent solution was heated at 80 ℃ in a water bath to produce a light yellow transparent gel, and the gel was further dried

at 120 ℃ in oven for 15 h to obtain yellow and dried gel. In the last step, the dried gel was annealed at 950 ℃ for 12 h in air to obtain the white phosphor powder. The Y_2SiO_5:Eu powder was also prepared for a comparison using the same method. The tetraethoxysilane (A.R. grade) was used as the source of silicon. The obtained powder was then reconstituted into micrometer-sized granules using polyving akohol. The finished powder has particle size varying between 50-100 μm with free-flowing for plasma spraying.

The phosphor specimens were prepared by air plasma spraying system on commercial Hastelly-X alloy substrates of a thickness of 4 mm. The substrates were ultrasonically cleaned, grit blasted with alumina mesh and then placed in the spraying system for overlying with coatings. The coating system consists of a NiCoCrAlY bond coat following by a 50 μm overcoat of the phosphor layer. The spray parameters are given in Table 1.

Table 1. Air plasma spray parameters for bond coat and phosphor layer depositions

Spray parameters	Bond coat	Phosphor layer
Spray distance (mm)	100	90
Arc current (A)	400	420
Voltage (V)	144	148
Ar flow rate (SLPM)	91.5	110
H_2 flow rate (SLPM)	15.9	20
Carrier gas flow rate (SLPM)	300	300
Gun speed (mm/s)	800	500

SLPM=Standard litres per minute

The crystal structures of the obtained phosphor layers were identified by X-ray diffraction (XRD, Rigaku) with CuKα radiation. Two theta angle from 10 °to 80 °was recorded with a scanning speed of 2 °/min. The microstructures of the phosphor layers were examined using scanning electron microscopy (SEM, FEI Quanta 200).

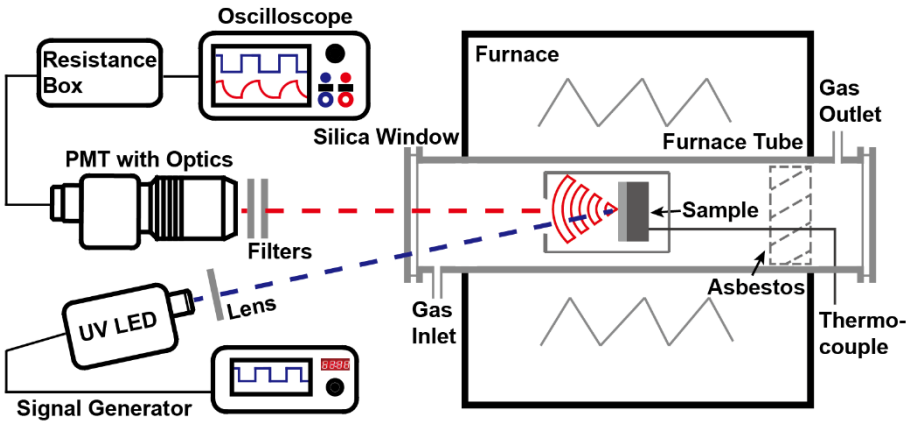

Fig. 1 Schematic of the experimental set up used to investigate the decay lifetimes and intensities of the selected phosphor layers in a pressure chamber. For an observation of the phosphorescent spectra, the PMT with optics was replaced by a spectrometer.

The phosphorescent properties of the excited phosphor layer were obtained using the set-up shown in Fig.1. The specimen was placed in a pressure chamber in which specimen could be heated in a controlled ambient gas of different oxygen concentration and the phosphorescence recorded simultaneously. The chamber was built using a furnace tube closed at both ends by a removable stainless steel flange, a gasket and a fused silica window. The flanges were equipped with four connections for gas inlet, gas outlet, pressure gage and thermocouple. The chamber was mounted concentrically within a high temperature tube furnace (SGL-1400, SIOMM) with a working temperature range of room temperature to 1250 ℃ and an accuracy of ±2 ℃. A K-type thermocouple (0-1090 ℃, ± 1%) was placed close to the specimen to monitor the temperature during the measurement. Insulation material (asbestos) was mounted on one end of the tube to improve the temperature uniformity within the furnace.

To achieve varying gas phase conditions, an open system was realized applying a continuous gas flow, controlled by gas flowmeter distant from the furnace at room temperature. Three different ambient oxygen concentrations (100, 20.95 and 0 %) were achieved by flowing three types of gas phase: high-purity oxygen, air and high-purity nitrogen with 1.5% methane. The methane was used to consume the residual oxygen in the chamber to achieve oxygen-free atmosphere by chemical reactions between oxygen

and methane at sufficiently high temperatures. Since this effect was not enhanced at higher methane concentrations, it is assumed that almost all oxygen was consumed at a content of 1.5%. All the measurements were made at a total chamber pressure of 1 atm but with different oxygen concentrations. To achieve higher purity of oxygen or oxygen-free ambient, the chamber was first evacuated and then filled with gas phase. This evacuating-filling procedure was repeated for 3 times at each designed temperatures.

The specimen was excited using a 405 nm diode laser being modulated by a function generator (Tektronix, AFG1022). This portable, low-cost laser could be modulated up to 30 kHz, which greatly improved the overall sampling rate. This is especially useful at high temperatures where the average of multiple measurements is usually required for achieving a sufficient signal-to-noise ratio. The phosphorescent signal was collected by a PMT (Photo Multiplier Tube) module (Hamamatsu, h9305-03) through a camera lens (Nikon 60 mm, f/2.8). A band-pass filter (600 nm +/− 25 nm) was installed before the camera lens to exclude the excitation light and reduce the thermal radiation at high temperatures. The current signal from the PMT was converted to voltage through a resistance box (R = 1 kΩ) and then recorded by an oscilloscope (Tektronix, DPO2002B) with a sampling rate of 3.125 MHz. For each measurement, the PMT signal was averaged over 512 laser pulses to ensure a good signal-to-noise ratio. The measurements at different temperatures were conducted after the temperature was stable. For the observation of phosphorescent spectra, the PMT system was replaced by an Ocean Optics USB 2000 grating spectrometer.

3 Data processing

Fig.2 (a) shows an excitation pulse (in blue) and sample decay curves of 0YSZ:Eu, 8YSZ:Eu, 12YSZ:Eu and $Zr_3Y_4O_{12}$:Eu following excitation at 405 nm recorded by the oscilloscope at room temperature. The features of phosphorescent decays can be identified using the curve of logarithm of intensity, as shown in Fig.2 (b). It can be seen that all of the phosphors display a single-exponential decay [12]. The single-

exponential decay was fitted using the function:

$$I = I_0 \cdot \exp(-t/\tau) \tag{1}$$

where τ is the lifetime of the phosphor, I is the measured intensity decay and I_0 is the intensity at the start of the decay.

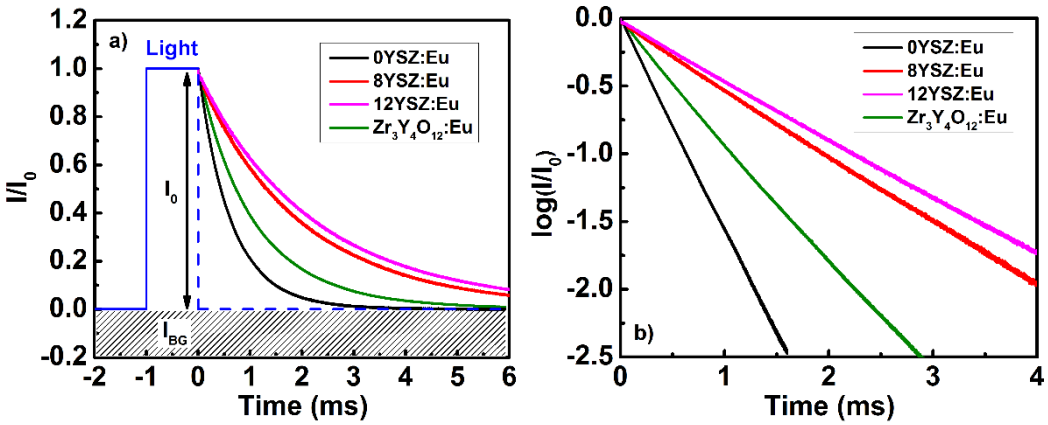

Fig. 2 (a) Schematic of an excitation pulse (in blue) and decay curves of 0YSZ:Eu, 8YSZ:Eu, 12YSZ:Eu and $Zr_3Y_4O_{12}$:Eu phosphor layers recorded by the oscilloscope, where I_{BG} is the background radiation level (in shaded area), I_0 is the intensity at the start of the luminescence decay $t = 0$. (b) Curves of logarithm of intensity with time.

The standard approach for calculating τ includes three steps: the background subtraction, the intensity normalization and the curve-fitting. The background level (I_{BG}) was evaluated using the average of intensities immediately before the start of the excitation pulse, as shown by the grey shaded area in Fig.2 (a). This background value (I_{BG}) was subtracted from the intensity data during the luminescent decay. Then all decay data were normalized by the intensity value (I_0). Finally, the intensity was fitted using the Eq.(1). Because the values obtained from the exponential fits can be sensitive to the choice of the start and end of fitting window, a precisely defined time window, which is only related to the decay time and independent of the settings of the acquisition system, is required [13, 14]. In this study, the fitting window starts at and ends at 0.5 times and 4.5 times of decay time, respectively, which yielded good results [13].

4. Results

4.1 Microstructure characterization and phase identification

Fig.3 shows the typical cross-sectional SEM image of the 8YSZ:Eu specimen consisting of a phosphor layer with approximately 50 μm thickness and a NiCoCrAlY bond coat with approximately 100 μm thickness on the top of the substrate. The microstructures of the four specimens with different Y^{3+}-doping levels are similar except the contrast in back scatter mode of the phosphor layers, due to the difference in their atomic masses.

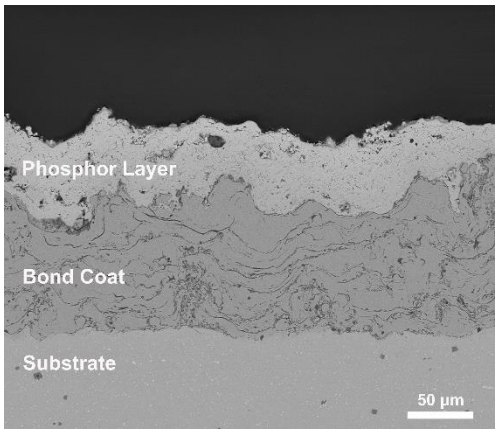

Fig. 3 Typical cross-sectional SEM image of the 8YSZ:Eu specimen consisting of a phosphor layer with approximately 50 μm thickness and a NiCoCrAlY bond coat on top of substrate.

Fig. 4 (a) presents the X-ray diffraction patterns for the phosphor layers in a range of 2θ between 10° and 80°. The pattern of 0YSZ:Eu has indicative monoclinic peaks at 28.0 °and 31.3 °for the (111) reflection. The peaks emerging in 30.2 °, 34.5 °, 50.2 °and 60.2 °angles for both of 8YSZ:Eu and 12YSZ:Eu represent the cubic phase and also show the tetragonal phase. Therefore, the enlarge XRD patterns in a range of 2θ between 72 °and 76 °were used to identify the tetragonal and cubic phases of 8YSZ:Eu and 12YSZ:Eu, as shown in Fig.4 (b). A doublet peak indicates a single-tetragonal crystal structure for the 8YSZ:Eu. The presence of a singlet of 12YSZ:Eu shows exclusively the formation of the cubic phase. To better display the extra diffraction

feature, the XRD pattern of $Zr_3Y_4O_{12}$:Eu is plotted on a logarithmic scale (Fig.4 (c)). The pattern clearly shows many extra diffraction lines, like the peaks of δ (110), δ (012), δ (220), δ (131), δ (303), δ (232) and δ (125). It suggests that the $Zr_3Y_4O_{12}$:Eu is order δ-phase. This phase consists of a hexagonal crystal structure, but its true symmetry is rhombohedral [15, 16]. If the symmetries of the crystal structures are compared, the following trend for the symmetry is obtained: 0YSZ:Eu (m) < $Zr_3Y_4O_{12}$:Eu (δ) < 8YSZ:Eu (t) <12YSZ:Eu (c). Since the Eu^{3+} ions substitute the Zr^{4+} ion in the crystalline lattice, the site symmetries of Eu^{3+} in the monoclinic, tetragonal and cubic phases are C_1, D_{2d} and O_h, respectively [17]. However, the site symmetry of Eu^{3+} in the $Zr_3Y_4O_{12}$:Eu is still unknown since that its complete cation ordering has so far eluded experimental identification [16].

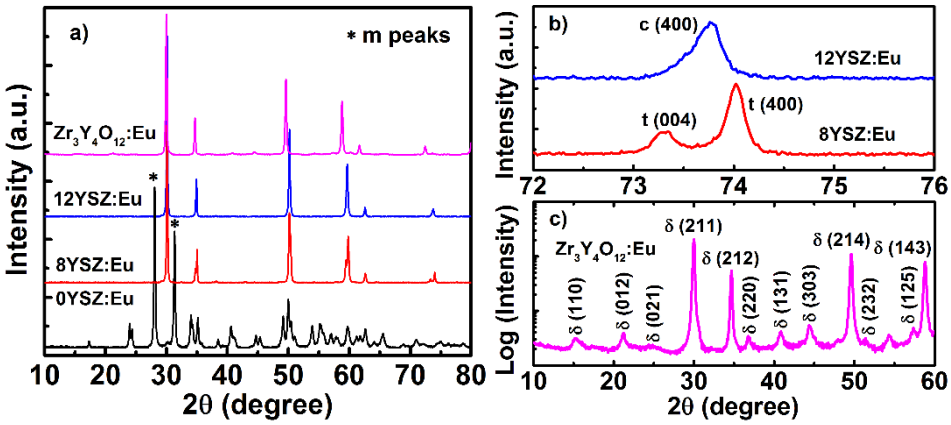

Fig. 4 Typical XRD patterns of the 0YSZ:Eu, 8YSZ:Eu, 12YSZ:Eu and $Zr_3Y_4O_{12}$:Eu phosphor layers in the 10-80° 2θ range (a). m represents monoclinic phase. (b) Enlarged XRD patterns of the 8YSZ:Eu and 12 YSZ:Eu phosphor layers in the 72-76° 2θ range to identify the tetragonal and cubic phases. t and c represent tetragonal and cubic phases, respectively. (c) XRD pattern of $Zr_3Y_4O_{12}$:Eu phosphor layer in the 10-60° 2θ range plotted on a logarithmic scale. δ represents rhombohedral phase.

4.2 Phosphorescent spectra

Fig.5 shows the phosphorescent spectra of 0YSZ:Eu (m), 8YSZ:Eu (t), 12YSZ:Eu (c) and $Zr_3Y_4O_{12}$ (δ) phosphor layers excited at 405 nm. The natures of phases identified

by X-ray diffraction are noted corresponding to each composition. The phosphorescent bands are assigned to transitions of Eu^{3+} from the $^5D_0$ excited level to the ^7F_J multiplets (J = 0, 1, 2). The more intense bands are due to the $^5D_0 \rightarrow {}^7F_1$ and $^5D_0 \rightarrow {}^7F_2$ transitions, and the corresponding bands usually peak at 570-600 nm and 600-640 nm, respectively. The much weaker phosphorescence comes from $^5D_0 \rightarrow {}^7F_0$ transitions which peak at about 580 nm. The phosphorescent spectra for the four phosphors exhibit different characteristic features (number, relative intensities, and positions of bands), which reflect the local structural properties around Eu^{3+} [18]. The features are described in the following paragraphs and summarized in Table 2.

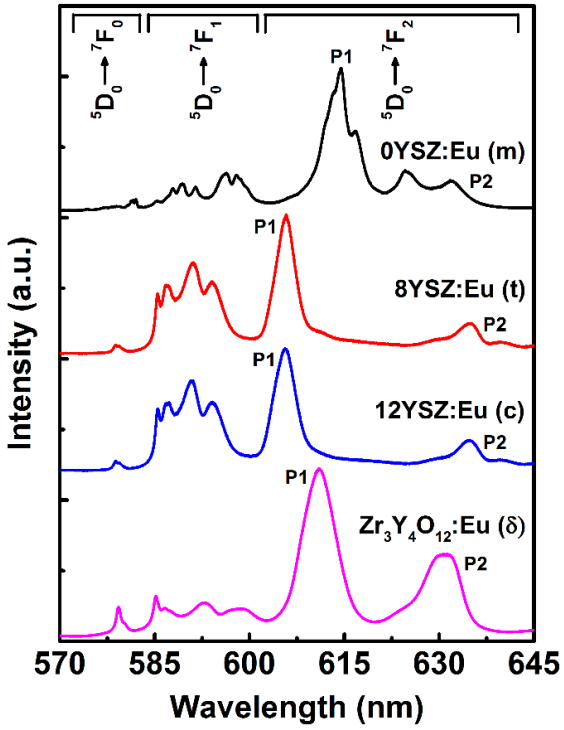

Fig. 5 Phosphorescent spectra of the 0YSZ:Eu (m), 8YSZ:Eu (t), 12YSZ:Eu (c) and $Zr_3Y_4O_{12}$:Eu phosphor layers excited at 405 nm. P1 and P2 represent the strongest and weaker bands from $^5D_0 \rightarrow {}^7F_2$ transition, respectively.

There is no significant change in the spectra of the 8YSZ:Eu (t) and 12YSZ:Eu (c) as the crystal structure evolved from tetragonal to cubic, which is consistent with results of the previous works [19, 20]. Both of their spectra consist of one line for $^5D_0 \rightarrow {}^7F_0$, four splitted lines for $^5D_0 \rightarrow {}^7F_1$ and four splitted lines for $^5D_0 \rightarrow {}^7F_2$, although they

contain different symmetries at the Eu^{3+}.The spectrum of the $Zr_3Y_4O_{12}$:Eu (δ) consists of two lines for $^5D_0 \rightarrow {}^7F_0$, four lines for $^5D_0 \rightarrow {}^7F_1$ and four lines for $^5D_0 \rightarrow {}^7F_2$. Many additional lines appear for the monoclinic phosphor whose spectrum consists of three, eight and six lines for $^5D_0 \rightarrow {}^7F_0$, $^5D_0 \rightarrow {}^7F_1$ and $^5D_0 \rightarrow {}^7F_2$ transitions, respectively. In particular, the phosphorescent band from $^5D_0 \rightarrow {}^7F_2$ transition peaked at 614 nm splits into four bands. These additional bands are associated with lower symmetry around the Eu^{3+} [17-19].

It is noted that the $^5D_0 \rightarrow {}^7F_2$ and $^5D_0 \rightarrow {}^7F_1$ electronic transitions are characterized by ~~a~~ different mechanisms. $^5D_0 \rightarrow {}^7F_1$ is a magnetic dipole allowed transition and is most independent of the host material. $^5D_0 \rightarrow {}^7F_2$ corresponds to the electronic dipole transition whose integrated emission intensity depends strongly on the site symmetry of Eu^{3+}. For this reason, it is well known that the asymmetry ratio of the integrated intensities of the $^5D_0 \rightarrow {}^7F_2$ and $^5D_0 \rightarrow {}^7F_1$ transitions can be considered as an effective probe of the site symmetry in which Eu^{3+} is situated and can be expressed as [18]:

$$R = \frac{I\left({}^5\mathrm{D}_0 \rightarrow {}^7\mathrm{F}_2\right)}{I\left({}^5\mathrm{D}_0 \rightarrow {}^7\mathrm{F}_1\right)} \tag{2}$$

In particular, the larger *R* value corresponds to lower site symmetry of Eu^{3+}. The values of the asymmetry ratio *R* for the 0YSZ:Eu (m), 8YSZ:Eu (t), 12YSZ:Eu (c) and $Zr_3Y_4O_{12}$:Eu (δ) are 3.74, 1.40, 1.22 and 3.49, respectively. Therefore, the site symmetries of Eu^{3+} for the four phosphors can be arranged from the lowest to the highest are: 0YSZ:Eu (m) < $Zr_3Y_4O_{12}$:Eu (δ) < 8YSZ:Eu (t) <12YSZ:Eu (c). The order is the same with that of the symmetries of the crystalline lattices, suggesting that the local environment of the Eu^{3+} is strongly dependent to the host lattice. The local structure of Eu^{3+} in δ phase is more distorted than tetragonal and cubic phases and slightly less distorted than monoclinic phase.

Another parameter that is sensitive to the Eu^{3+} site symmetry is the peak position. As shown in Fig.5, it is clear that the $^5D_0 \rightarrow {}^7F_2$ transition bands (P1 and P2) shift with

variations in symmetry, while the $^5D_0 \rightarrow {}^7F_1$ transition seems unaffected. The strongest phosphorescence (P1) of the monoclinic, tetragonal, cubic and δ phase phosphors comes from $^5D_0 \rightarrow {}^7F_2$ transition peaking at 614.62, 605.68, 605.56 and 610.99 nm, respectively. Since that the band shifts to a shorter wavelength as the site symmetry of Eu^{3+} increases, which has been reported in previous works [21, 22], the peak position of P1 band is an additional evidence for the Eu^{3+} site symmetry order of the four phosphors, namely the Eu^{3+} site symmetry in the δ phase is higher for the monoclinic but lower than the tetragonal and cubic phases. In addition, the weaker phosphorescent bands from $^5D_0 \rightarrow {}^7F_2$ transition (P2) of the monoclinic, tetragonal, cubic and δ phase phosphors peaked at 624.67, 634.69, 634.78 and 630.72 nm, respectively. This suggests that the P2 band also shift with the site symmetry of Eu^{3+}, but is shifting to a longer wavelength as the site symmetry of Eu^{3+} increases. The origin of the shifts is not fully understood but is believed to be related to the volume difference of the unit cell between these four phases, which changes the mean magnitude of the crystal field felt by the electrons in the Eu^{3+} [22、23].

Table 2 Summary of the phosphorescent characteristics of the four Eu^{3+} doped YSZ phosphors excited at 405 nm

Samples	Phase	Eu^{3+} site symmetry	Peak number			Asymmetry ratio *R*	Peak position of P1	Peak position of P2
			$^5D_0 \rightarrow {}^7F_0$	$^5D_0 \rightarrow {}^7F_1$	$^5D_0 \rightarrow {}^7F_2$			
0YSZ:Eu	m	C_1	3	8	6	3.74	614.62	624.67
8YSZ:Eu	t	D_{2d}	1	4	4	1.40	605.68	634.69
12YSZ:Eu	c	O_h	1	4	4	1.22	605.56	634.78
$Zr_3Y_4O_{12}$:Eu	δ	unknown	2	4	4	3.49	610.99	630.72

4.3 Phosphorescence variations with temperature and oxygen concentration

Fig.6 (a-d) shows the lifetime-temperature curves obtained in three different gas phase conditions (air, O_2 and 1.5% CH_4/98.5% N_2) at ambient pressure for the 0YSZ:Eu (m),

8YSZ:Eu (t), 12YSZ:Eu (c) and $Zr_3Y_4O_{12}$:Eu (δ) phosphor layers. Measurements of phosphorescent lifetimes were taken up to temperatures at which the intensity of the phosphorescent signals fell below the noise floor. The lifetime variations with temperature for all the phosphors exhibit the same characteristic of a relatively constant value from room temperature up to an intermediate temperature (namely the quenching temperature) and thereafter an exponential decrease as temperature increases.

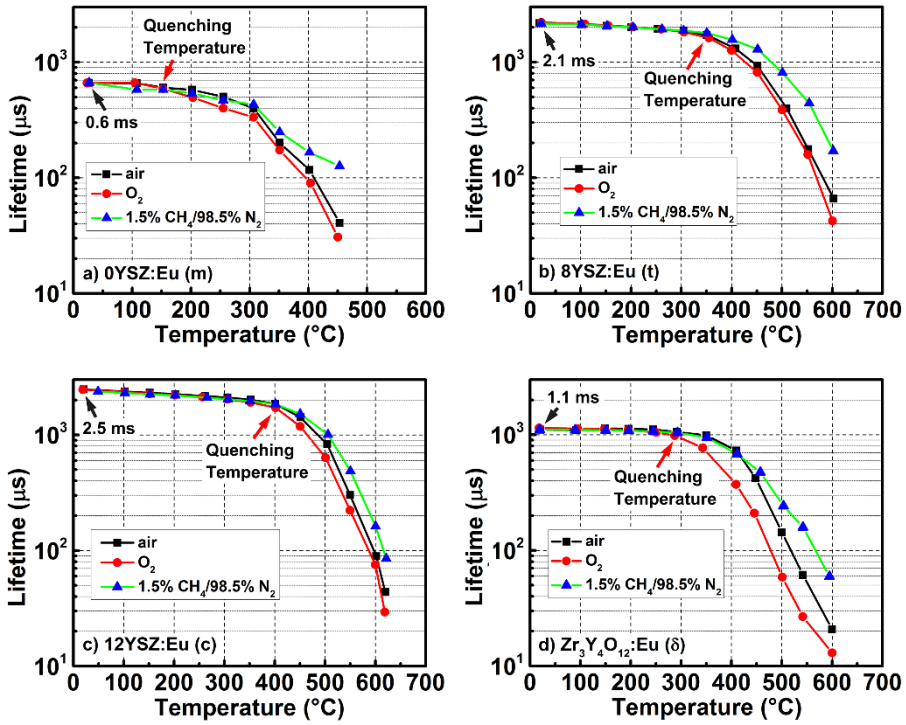

Fig. 6 Phosphorescent lifetime-temperature curves obtained in three different gas phases (air, O_2 and 1.5% CH_4/98.5% N_2) at ambient pressure for the 0YSZ:Eu (m), 8YSZ:Eu (t), 12YSZ:Eu (c) and $Zr_3Y_4O_{12}$:Eu (δ) phosphor layers.

There are two notable features observed from Fig.6. One is the lifetime values measured in air reveal some interesting correlations with the site symmetry of Eu^{3+}. Different levels of Eu^{3+} site symmetry give rise to different phosphorescent lifetimes, even for the 8YSZ:Eu (t) and 12YSZ:Eu (c), which have no significant difference in the phosphorescent spectra. Firstly, the lifetime values at low temperature (the flat portions of the lifetime-temperature curves) increase with the site symmetry of Eu^{3+}, which is because of relaxation in La-Porte selection rule [24]. Secondly, the quenching

temperatures for the monoclinic, tetragonal, cubic and δ phase phosphors are about 150, 350, 400 and 300 ℃, respectively. This suggests that increasing the site symmetry of Eu^{3+} also shifts the onset of thermal quenching to a higher temperature. In addition, there is no obvious difference in the curve slope, which determines the temperature sensitivity.

Another striking finding from Fig.6 is that the oxygen concentration strongly influences the phosphorescence lifetime above the onset temperature of thermal quenching. The lifetime decreases with increasing ambient oxygen concentration at a constant temperature, showing an oxygen quenching behavior similar to organic luminophores. As a result, the curves are shifted to lower temperatures at higher ambient oxygen concentration. In contrast, when the temperature is lower than the quenching temperature, the lifetime is not influenced by the ambient oxygen concentration. The phosphorescent intensity-temperature curves for the four phosphor layers at different ambient oxygen concentrations are also illustrated in Fig.7 (a-d). The intensities are normalized by the intensity at room temperature for each specimen. It is clear that the

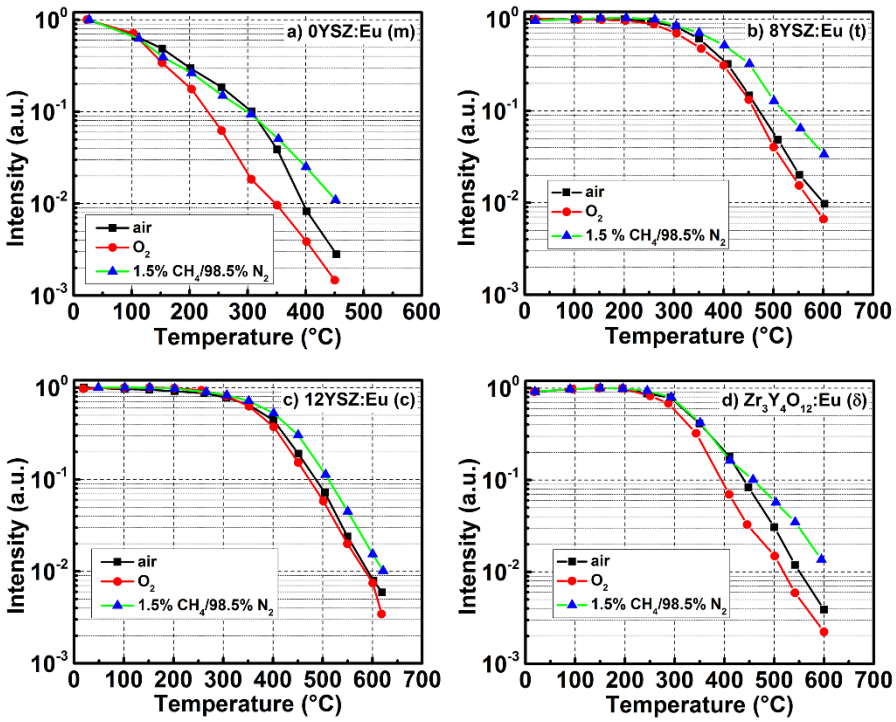

Fig. 7 Phosphorescent intensity-temperature curves obtained in three different gas phases (air, O_2

and 1.5% CH_4/98.5% N_2) at ambient pressure for the 0YSZ:Eu (m), 8YSZ:Eu (t), 12YSZ:Eu (c) and $Zr_3Y_4O_{12}$:Eu (δ) phosphor layers.

intensity exhibits the oxygen quenching behavior very similar to the lifetime. The mechanisms responsible for this oxygen quenching behavior will be discussed in the next section.

5 Discussion

5.1 Mechanisms of the "oxygen quenching"

The principal finding of this work is that the ambient oxygen concentration has a significant influence on the phosphorescent lifetimes and intensities for the four Eu-doped YSZ phosphors. The "oxygen quenching" of lifetime is similar to the results shown in the previous work by Brübach *et al*. (high oxygen sensitivity of Y_2O_3:Eu) [10]. Meanwhile, in their study, other two phosphors (La_2O_2S:Eu and Mg_4FGeO_6:Mn) were found to be insensitive to the ambient oxygen concentration. Comparing these two phosphors with the five known oxygen-sensitive phosphors (0YSZ:Eu, 8YSZ:Eu, 12YSZ:Eu, $Zr_3Y_4O_{12}$:Eu and Y_2O_3:Eu), it appears that the main difference between them is whether there are pre-existing oxygen vacancies in their host lattices:

i) When the lower-valent oxides (Y_2O_3 and Eu_2O_3) are doped into ZrO_2, the Zr^{4+} ions are replaced by the Y^{3+} or Eu^{3+} ions, and oxygen vacancies are consequently generated in the anion sublattice to compensate the charge missing [25, 26]. The oxygen vacancy concentration increases with the dopant concentration. For the 0YSZ:Eu (m), 8YSZ:Eu (t) and 12YSZ:Eu (c), the oxygen vacancies are disorderly arranged. But for the $Zr_3Y_4O_{12}$:Eu (δ), oxygen vacancies lie along this specific [111] direction, resulting in infinite strings of 6-coordinated metal cations following the 3-fold axis [15, 27]. At elevated temperature, the ordered state of oxygen vacancies will transform to a disordered state.

ii) There are also oxygen vacancies in the Y_2O_3:Eu. The Y_2O_3 has the C-type cubic

crystal structure, which is described as a modified fluorite-type cubic structure with one fourth of the anion sites vacant and regularly arranged [28].

iii) La_2O_2S:Eu and Mg_2FGeO_6:Eu have hexagonal [29] and orthorhombic crystal structures [30], respectively. Both of them have no oxygen vacancy and show no oxygen sensitivity.

Therefore, to verify that whether the pre-existing oxygen vacancy is a prerequisite for oxygen quenching in phosphors, a reference phosphor layer (Y_2SiO_5:Eu) (without oxygen vacancy) was prepared and tested. Y_2SiO_5 crystallizes in the B2/b space group with a monoclinic structure [31]. There are four types of oxygen sites (O_1-O_4) in the SiO_4 tetrahedron and one type of interstitial non-silicon-bonded oxygen site (O_5) surrounded by four Y atoms [31]. The lifetime-temperature curves obtained in three different gas phase conditions (air, O_2 and 1.5% CH_4/98.5% N_2) at ambient pressure for the Y_2SiO_5:Eu phosphor layer are shown in Fig. 8. It is evident that its phosphorescent lifetimes are not influenced by the ambient oxygen concentration, which suggests that the oxygen vacancy is essential for the oxygen sensitivity of phosphors. This "oxygen quenching" mechanism due to oxygen vacancy is explained in detail in the following paragraphs.

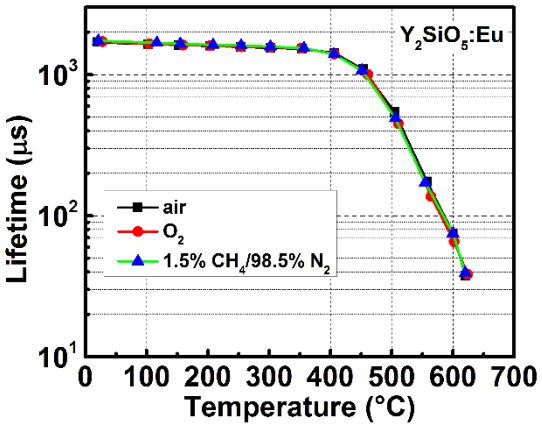

Fig. 8 Phosphorescent lifetime-temperature curves obtained in three different gas phases (air, O_2 and 1.5% CH_4/98.5% N_2) at ambient pressure for the Y_2SiO_5:Eu phosphor layer.

For the phosphors in which the oxygen vacancies are in solution on the oxygen sublattice, the oxygen vacancy concentration varies with the ambient gas due to the exchange of oxygen between the crystal lattice and the high-temperature gas. This process can be expressed as [25]:

$$O_O^{\times} = 1/2O_2(\text{gas}) + V_O^{\bullet\bullet} + 2e' \quad (3)$$

For the phosphors without pre-existing oxygen vacancies, the oxygen vacancy concentration is almost unchanged with the variation of the ambient gas. It should be noted that oxygen vacancies are supposed to form at high temperature for the Y_2SiO_5:Eu. But it has a high activation energy for self-diffusion which leads to extremely low oxygen permeability [31]. Therefore, the oxygen vacancy concentration in the lattice is hardly changed with the ambient gas. Considering that the high oxygen ionic conductivity due to the presence of a large number of oxygen vacancies [26] and the translucent nature of the ceramic YSZ to the visible light [5, 7], it is not only the oxygen vacancies on the surface of the phosphor layer that should be considered, but also those in the inner part.

The phosphorescent lifetime equals the inverse of the sum of the radiative and non-radiative decay rates. Since the radiative decay rate remains relatively constant over all measurements for a certain phosphor, the lifetime is largely controlled by the non-radiative decay rate. According to the lifetime results in Fig.6, the oxygen quenching occurs when the temperature is over the quenching temperature and the lifetime increases as the oxygen vacancy concentration increases (due to reduced ambient oxygen concentration) in the lattice, suggesting that the oxygen vacancies decrease the non-radiative decay rate. The reason for this phenomenon can be explain as follows. The dominant non-radiative transitions in YSZ:Eu materials are charge-transfer states (CTS) processes [11]. The oxygen vacancies can act as electron trap sites for the electrons generated by excitation [32, 33]. These trap sites could prevent the extra electrons from migrating and combining non-radiatively with trapped holes. Namely,

the presence of oxygen vacancies causes CTS to shift in the configuration coordinate diagram due to its changed environment [33-35]. As a result of this shift, the barrier against the non-radiative transition becomes higher and hence the phosphorescent intensities get stronger and the lifetimes get longer.

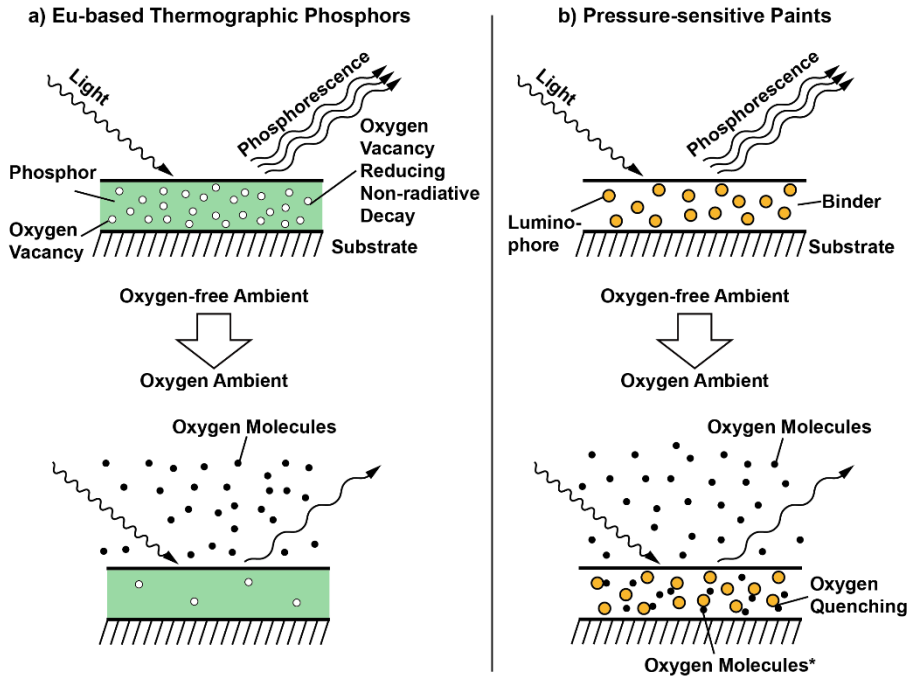

Fig. 9 Schematic diagrams of the "oxygen quenching" mechanism for the Eu-based thermographic phosphors (a) and the oxygen quenching mechanism for the pressure-sensitive paints (b). Oxygen molecules are excited once they quench phosphorescence. * denotes the excited state.

In summary, for the Eu-based phosphors, the "oxygen quenching" is essentially a two-step process: i) increased ambient oxygen concentration leads to reduction in oxygen vacancies in the lattice; ii) the non-radiative decay is enhanced by a lower concentration of oxygen vacancy. This mechanism is entirely different from the typical oxygen quenching in organic luminophores where the oxygen molecules directly promote the non-radiative decay through the formation of singlet oxygen. Schematic diagrams of these two mechanisms are shown in Fig. 9(a-b). Therefore, oxygen quenching is not correct to describe this phenomenon of the Eu^{3+}-based thermographic phosphors and double quotes are used in the current paper to indicate the distinction.

In addition, Fig.6 shows that the lifetimes decrease exponentially with temperature above the quenching temperature for all phosphors under all atmospheres. This phenomenon in air has been reported by previous works [7, 36]. Since the relationship between the non-radiative decay rate and the temperature is unchanged with different ambient, the lifetime also decreases exponentially with temperature above the quenching temperature under other atmospheres.

5.2 Ambient oxygen concentration sensitivity

As shown in Fig.6 and Fig. 8, the phosphorescent lifetimes for the five phosphor layers (0YSZ:Eu, 8YSZ:Eu, 12YSZ:Eu, $Zr_3Y_4O_{12}$:Eu and Y_2SiO_5:Eu) exhibit different ambient oxygen concentration sensitivities. Since the lifetime-temperature curves were only measured in three ambient gases, the oxygen sensitivity is evaluated by:

$$S_{O_2} = \frac{\tau_{CH_4/N_2}}{\tau_{O_2}} \tag{4}$$

where S_{O_2} is the ambient oxygen concentration sensitivity; τ_{CH_4/N_2} and τ_{O_2} are the lifetimes measured in the nitrogen with methane and oxygen ambient, respectively. The sensitivity values of the five phosphor layers are presented in Fig.10. It can be seen

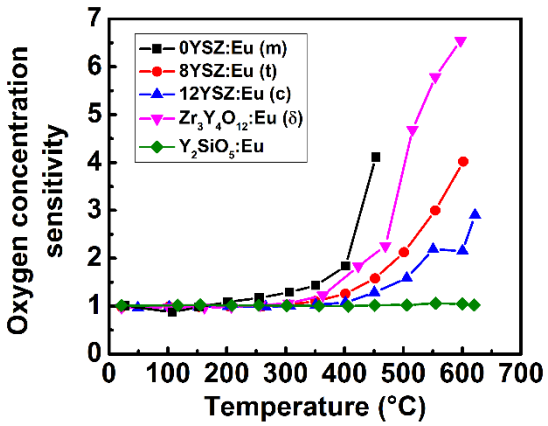

Fig. 10 Oxygen concentration sensitivities of the 0YSZ:Eu (m), 8YSZ:Eu (t), 12YSZ:Eu (c) and $Zr_3Y_4O_{12}$:Eu (δ) phosphor layers compared with that of the reference Y_2SiO_5:Eu phosphor layer as a function of temperature.

that the oxygen sensitivity decreases in the following order at a certain temperature: 0YSZ:Eu (m) > $Zr_3Y_4O_{12}$:Eu (δ) > 8YSZ:Eu (t) > 12YSZ:Eu (c), while the Y_2SiO_5:Eu has no oxygen sensitivity. Interestingly, this trend is directly opposite to that of the site symmetry of Eu^{3+} (from low to high), suggesting that a lower site symmetry of Eu^{3+} leads a higher oxygen sensitivity. Meanwhile, there is no clear relationship between the oxygen sensitivity and the pre-existing oxygen vacancy concentration, which increases in the order: 0YSZ:Eu (m), 8YSZ:Eu (t), 12YSZ:Eu (c) and $Zr_3Y_4O_{12}$:Eu (δ) due to the increase of dopant concentration. The oxygen sensitivities of the 0YSZ:Eu (m) and the $Zr_3Y_4O_{12}$:Eu (δ) phosphors as oxygen sensors are comparable to that of the Y_2O_3:Eu phosphor studied by previous work [10].

As shown in Fig.6, the quenching temperature increases with the site symmetry of Eu^{3+} in air. This suggests that the phosphor with a lower site symmetry has a lower CTS energy [37]. Moreover, the low site symmetry also broadens the CTS band [34]. Both effects tend to enhance the non-radiative decay [37], namely the non-radiative decay takes a larger proportion of the total decay at a certain temperature. Therefore, the emission of phosphor with lower site symmetry is more susceptible to oxygen vacancies due to its strong non-radiative decay. In addition, Fig.10 shows that the sensitivity increases with temperature. This is because that the non-radiative decay by CTS processes is thermally promoted [37]. A high temperature leads to a high proportion of non-radiative decay. As a result, the reduction of non-radiative decay rate by oxygen vacancies will become larger at high temperature.

5.3 Potential application in oxygen/pressure sensing

Based on the previous discussion, the existence of oxygen vacancies decides whether the Eu^{3+} ions are sensitive to the ambient oxygen concentration, and the site symmetry of Eu^{3+} strongly affects the oxygen sensitivity. These findings can provide guidelines for materials selection and sensor design for potential applications of oxygen/pressure sensing in high-temperature environment. Since the lifetime of Eu^{3+} is influenced by both the temperature and the ambient oxygen concentration, a calibration map (three

dimensional plot showing the lifetime versus the temperature and the ambient oxygen concentration) can be generated. Using this map, the oxygen concentration and/or surface pressure can be determined by measurement of the phosphorescent lifetimes at known temperatures. More importantly, it is possible to combine an oxygen-sensitive coating with a second thermographic phosphor without oxygen sensitivity, forming a dual-sensor system similar to the two-color PSP used in aerodynamic research [38]. In this way, both of the oxygen concentration/pressure and the temperature can be obtained simultaneously using a color camera or a two camera system. This opens possibilities of surface pressure and temperature measurements in high-temperature environment that are desired in many scenarios of aerodynamic research. For example, the pressure loads, surface temperatures and heat fluxes are critical parameters in studies of jet impingement, turbomachinery, reentry objects and hypersonic aircrafts [39-41].

6 Conclusions

In this study, the effect of ambient oxygen concentration on the temperature-dependent phosphorescent properties (lifetime and intensity) of the four Eu^{3+} doped YSZ thermographic phosphor layers (with monoclinic, tetragonal, cubic and δ phases, respectively) was studied. The phosphors were prepared using sol-gel method by controlling the Y^{3+} concentrations of 0, 8, 12, 57 mol% and the phosphor layers were deposited using APS process. The main findings are summarized as follows:

i) The phosphorescent spectra appeared to be markedly different for the four phosphors. Based on the spectral features (number, asymmetry ratio and position of bands), the site symmetry of Eu^{3+} for the phosphors increased in the following order: monoclinic 0YSZ:Eu, δ $Zr_3Y_4O_{12}$:Eu, tetragonal 8YSZ:Eu and cubic 12YSZ:Eu.

ii) The phosphorescent lifetimes were also dependent on the Eu^{3+} site symmetry: (a). the phosphorescent lifetimes at the low temperature (lower than the quenching temperature) increased with the site symmetry of Eu^{3+}; (b). a high site symmetry of Eu^{3+} contributed to a high quenching temperature, which was also observed from the

phosphorescent intensity results.

iii) The phosphorescent lifetimes and intensities for the four phosphors were sensitive to the ambient oxygen concentration. As the ambient oxygen concentration increased, the lifetimes and intensities of the phosphors decreased, showing an "oxygen quenching" phenomenon. This only occurred when the temperature was higher than the quenching temperature. The phosphorescent lifetimes of Y_2SiO_5:Eu were not influenced by the ambient oxygen concentration.

iv) The sensitivity to the ambient oxygen concentration was attributed to the existence of oxygen vacancies in the host lattice. The oxygen vacancy could shift the CTS in the configuration-coordinate diagram and reduced the non-radiative decay. The variation of oxygen vacancy concentration with ambient oxygen concentration contributed to the change of the strength of this reduction and consequently changed the phosphorescent lifetime and intensity.

v) The ambient oxygen concentration sensitivities of the phosphors decreased in the following order: monoclinic 0YSZ:Eu, δ $Zr_3Y_4O_{12}$:Eu, tetragonal 8YSZ:Eu and cubic 12YSZ:Eu. The sensitivity was found to be closely related to the site symmetry of Eu^{3+}. Low site symmetry led to CTS bands broadening and CTS energy reduction. As a result, the non-radiative decay became stronger with increased oxygen sensitivity since the non-radiative process was affected by oxygen vacancies.

Acknowledgements

The authors would thank the financial support from Siemens Ltd., China, the "1000 Plan Program", the Program for Professor of Special Appointment (Eastern Scholar) at Shanghai Institutions of Higher Learning (No.SHDP201303), the National Natural Science Foundation of China (Nos.51271120 and 51402058), and the fund of Shanghai Committee of Science and Technology (No. 14ZR142).

References

[1] S.W. Allison, G.T. Gillies, Remote thermometry with thermographic phosphors: Instrumentation and applications, Rev. Sci. Instrum. 68 (1997) 2615.

[2] M. Aldén, A. Omrane, M. Richter, G. Särner, Thermographic phosphors for thermometry: a survey of combustion applications, Prog. Energy Combust. Sci. 37 (2011) 422-461.

[3] A.H. Khalid, K. Kontis, Thermographic phosphors for high temperature measurements: principles, current state of the art and recent applications, Sens. 8 (2008) 5673-5744.

[4] J.P. Feist, A.L. Heyes, Photo-stimulated phosphorescence for thermal condition monitoring and nondestructive evaluation in thermal barrier coatings, Heat Transfer Eng. 30 (2009) 1087-1095.

[5] L. Yang, D. Peng, C. Zhao, C. Xing, F. Guo, Z. Yao, Y. Liu, X. Zhao, P. Xiao, Evaluation of the in-depth temperature sensing performance of Eu-and Dy-doped YSZ in air plasma sprayed thermal barrier coatings, Surf. Coat. Technol. 316 (2017) 210-218.

[6] S.J. Yi, K.C. Kim, Phosphorescence-based multiphysics visualization: a review, J. Visual. 17 (2014) 253-273.

[7] M.D. Chambers, D.R. Clarke, Doped oxides for high-temperature luminescence and lifetime thermometry, Annu. Rev. Mater. Res. 39 (2009) 325-359.

[8] T. Liu, J.P. Sullivan, Pressure and temperature sensitive paints (2005)[J], ed: Springer, Berlin, DOI (2005).

[9] J. Feist, A. Heyes, S. Seefeldt, Oxygen quenching of phosphorescence from thermographic phosphors, Meas. Sci. Technol. 14 (2003) N17.

[10] J. Brübach, A. Dreizler, J. Janicka, Gas compositional and pressure effects on thermographic phosphor thermometry, Meas. Sci. Technol. 18 (2007) 764.

[11] Y. Shen, D.R. Clarke, Effects of Reducing Atmosphere on the Luminescence of Eu3+ - Doped Yttria - Stabilized Zirconia Sensor Layers in Thermal Barrier Coatings, J. Am. Ceram. Soc. 92 (2009) 125-129.

[12] J. Liao, D. Zhou, B. Yang, R. Liu, Q. Zhang, Sol–gel preparation and photoluminescence properties of tetragonal ZrO2: Y3+, Eu3+ nanophosphors, Opt. Mater. 35 (2012) 274-279.

[13] K. C, L. J, A.N. F, R. M, A. M, Investigation and compensation of the nonlinear response in photomultiplier tubes for quantitative single-shot measurements, Rev. Sci. Instrum. 83 (2012) 034901.

[14] J. Brübach, J. Feist, A. Dreizler, Characterization of manganese-activated magnesium fluorogermanate with regards to thermographic phosphor thermometry, Meas. Sci. Technol. 19 (2008) 025602.

[15] C. Pascual, P. Duran, Subsolidus Phase Equilibria and Ordering in the System ZrO2 - Y2O3, J. Am. Ceram. Soc. 66 (1983) 23-27.

[16] G.P. Cousland, X.Y. Cui, S. Ringer, A.E. Smith, A.P.J. Stampfl, C.M. Stampfl, Electronic and vibrational properties of yttria-stabilised zirconia from first-principles for 10–40mol% Y2O3, J. Phys. Chem. Solids 75 (2014) 1252-1264.

[17] A. Speghini, M. Bettinelli, P. Riello, S. Bucella, A. Benedetti, Preparation, structural characterization, and luminescence properties of Eu3+-doped nanocrystalline ZrO2, J. Mater. Res. 20 (2011) 2780-2791.

[18] K. Smits, L. Grigorjeva, D. Millers, A. Sarakovskis, A. Opalinska, J.D. Fidelus, W. Lojkowski, Europium doped zirconia luminescence, Opt. Mater. 32 (2010) 827-831.

[19] J. Dexpert-Ghys, M. Faucher, P. Caro, Site selective spectroscopy and structural analysis of yttria-doped zirconias, J. Solid State Chem. 54 (1984) 179-192.

[20] M.M. Gentleman, High temperature sensing of thermal barrier materials by luminescence[M] ProQuest, Ph.D. Dissertation, University of California (2006).

[21] Z. Wei, L. Sun, C. Liao, J. Yin, X. Jiang, C. Yan, S. Lü, Size-dependent chromaticity in YBO3: Eu nanocrystals: correlation with microstructure and site symmetry, J. Phys. Chem. B 106 (2002) 10610-10617.

[22] Y. Hui, Y. Zhao, S. Zhao, L. Gu, X. Fan, L. Zhu, B. Zou, Y. Wang, X. Cao, Fluorescence of Eu3+ as a probe of phase transformation of zirconia, J. Alloys Compd. 573 (2013) 177-181.

[23] J. Moon, H. Choi, H. Kim, C. Lee, The effects of heat treatment on the phase transformation behavior of plasma-sprayed stabilized ZrO2 coatings, Surf. Coat. Technol. 155 (2002) 1-10.

[24] S.K. Gupta, C. Reghukumar, R.M. Kadam, Eu3+ local site analysis and emission characteristics of novel Nd2Zr2O7:Eu phosphor: insight into the effect of europium concentration on its photoluminescence properties, RSC Adv. 6 (2016) 53614-53624.

[25] Y. Wang, Effect of reduction treatment on microstructure and mechanical properties of fluorite oxides, Ph.D. Dissertation, University of Florida (2006).

[26] F. Yang, Electrical and thermal properties of yttria-stabilised zirconia (YSZ)-based ceramic materials, Ph.D. Dissertation, University of Manchester (2011).

[27] V.S. Stubican, R.C. Hink, S.P. Ray, Phase Equilibria and Ordering in the System ZrO2 - Y2O3, J. Am. Ceram. Soc. 61 (1978) 17-21.

[28] K. Ando, Y. Oishi, H. Hase, K. Kitazawa, Oxygen Self - Diffusion in Single - Crystal Y2O3, J. Am. Ceram. Soc. 66 (1983).

[29] Q.L. Dai, H.W. Song, M. Wang, X.D. Bai, B. Dong, R.F. Qin, X. Qu, H. Zhang, Size and Concentration Effects on the Photoluminescence of La2O2S:Eu3+ Nanocrystals, J. Phys. Chem. C 112 (2008) 19399-19404.

[30] R.B. Von Dreele, P.W. Bless, E. Kostiner, R.E. Hughes, The crystal structure of magnesium germanate: A reformulation of Mg4GeO6 as Mg28Ge10O48, J. Solid State Chem. 2 (1970) 612-618.

[31] B. Liu, J. Wang, F. Li, J. Wang, Y. Zhou, Mechanisms of Mono - Vacancy and Oxygen Permeability in Y2SiO5 Orthosilicate Studied by First - Principles Calculations, J. Am. Ceram. Soc. 95 (2012) 1093-1099.

[32] F. Clabau, X. Rocquefelte, T. Le Mercier, P. Deniard, S. Jobic, M.H. Whangbo, Formulation of phosphorescence mechanisms in inorganic solids based on a new model of defect conglomeration[J], Chem. Mater. 18 (2006) 3212-3220.

[33] K. Chae, T. Park, C.I. Cheon, N.I. Cho, J.S. Kim, Enhanced phase miscibility and luminescence by inducing oxygen vacancies in Ce1−xEuxO2−δ under a strongly reducing atmosphere, J. Lumin. 136 (2013) 109-116.

[34] K. Chae, T. Park, C.I. Cheon, N.I. Cho, J.S. Kim, Luminescence enhancement by the reduction–oxidation synthesis in monoclinic RE2O3(RE=Eu, Gd) phosphors containing Eu3+ activator, J. Lumin. 132 (2012) 2293-2301.

[35] C.W. Struck, W.H. Fonger, Dissociation of Eu+3 Charge-Transfer State in Y2O2S and La2O2S into Eu+2 and a Free Hole, Phys. Rev. B DOI (1971).

[36] Y. Shen, M.D. Chambers, D.R. Clarke, Effects of dopants and excitation wavelength on the temperature sensing of Ln3+-doped 7YSZ, Surf. Coat. Technol. 203 (2008) 456-460.

[37] R. Steenbakker, Phosphor thermometry in an EB-PVD TBC, Ph.D. Dissertation, University of Cranfield (2008).

[38] D. Peng, C.D. Jensen, T.J. Juliano, J.W. Gregory, J. Crafton, S. Palluconi, T. Liu, Temperature-compensated fast pressure-sensitive paint, AIAA J. 51 (2013) 2420-2431.

[39] D. Peng, L. Jiao, Z. Sun, Y. Gu, Y. Liu, Simultaneous PSP and TSP measurements of transient flow in a long-duration hypersonic tunnel, Exp. Fluids 57 (2016) 188.

[40] A.R. Khojasteh, S.F. Wang, D. Peng, S. Yavuzkurt, Y. Liu, Structure analysis of adiabatic film cooling effectiveness in the near field of a single inclined jet: Measurement using fast-response pressure-sensitive paint, Int. J. Heat Mass Transfer 110 (2017) 629-642.

[41] D. Peng, Y. Liu, A grid-pattern PSP/TSP system for simultaneous pressure and temperature measurements, Sens. Actuators B 222 (2016) 141-150.

Lixia Yang is currently pursuing for her Ph.D. under the supervision of Profs. Ping Xiao and Xiaofeng Zhao in School of Materials Science and Engineering, Shanghai Jiao Tong University, majoring in stress analysis and temperature sensing in thermal barrier coatings used for industrial gas-turbines.

Xiaofeng Zhao obtained his Ph.D. in Materials Science from the University of Manchester, UK, in 2007. He is currently an Associate Professor in School of Materials Science and Engineering, Shanghai Jiao Tong University. His research interests are the thermal barrier coatings used for industrial gas-turbines and aero-engines.

Di Peng received his Ph.D. in aerospace engineering from The Ohio State University in 2014. He is currently an assistant professor in School of Mechanical Engineering, Shanghai Jiao Tong University. His main research interest is pressure- and temperature-sensitive paints and their applications in aerodynamic testing.

Xiao Shan is currently a PhD candidate of School of Materials Science and Engineering in Shanghai Jiao Tong University, majoring in corrosion of thermal barrier coatings used for industrial gas-turbines and aero-engines.

Fangwei Guo received her Ph.D. in Science of Glasses & Ceramic from The University of Manchester in 2012. She is currently a lecturer in School of Materials Science and Engineering, Shanghai Jiao Tong University. Her main research interests are advanced fabrication of porous ceramic membranes/coatings and characterization of their thermal properties and fracture behaviors.

Yingzheng Liu received his Ph.D. in mechanical engineering from Shanghai Jiao Tong University in 2000. He is currently a professor in School of Mechanical Engineering, Shanghai Jiao Tong University. He also serves as vice dean for Gas Turbine Research Institute at SJTU. His research interest includes advanced measurement technologies of fluid mechanics (PDPA, PIV, LIF, PSV, PSP), turbulent flow and flow control, complex flow and heat transfer in turbo machinery, as well as bio-fluid mechanics.

Ping Xiao received his Ph.D. in Materials Science from the Oxford University in 1993.

He is currently a Professor in Materials Science Centre, University of Manchester. He also serves as a Visiting Professor in School of Materials Science and Engineering, Shanghai Jiao Tong University. His research area covers the thermal barrier coatings for aeroengines and power generation, and ceramic coatings for nuclear industry applications.